frontiers | Frontiers in Nanotechnology

TYPE Mini Review
PUBLISHED 29 January 2025
DOI 10.3389/fnano.2025.1537299

OPEN ACCESS

EDITED BY
Chiara Trovatello,
Columbia University, United States

REVIEWED BY
Yinan Dong,
Columbia University, United States
Sebastian Klimmer,
Friedrich Schiller University Jena, Germany

*CORRESPONDENCE
Ana M. de Paula,
ana@fisica.ufmg.br

†These authors have contributed equally to this work

RECEIVED 30 November 2024
ACCEPTED 10 January 2025
PUBLISHED 29 January 2025

CITATION
Sousa FB, Lafeta L, Fonseca GR and de Paula AM (2025) Nonlinear optical imaging of two-dimensional nanomaterials.
Front. Nanotechnol. 7:1537299.
doi: 10.3389/fnano.2025.1537299

Nonlinear optical imaging of two-dimensional nanomaterials

Frederico B. Sousa[1,2†], Lucas Lafeta[3†], Gladystone R. Fonseca[1] and Ana M. de Paula[1*]

[1]Departamento de Física, Instituto de Ciências Exatas, Universidade Federal de Minas Gerais, Belo Horizonte, Minas Gerais, Brazil, [2]Departamento de Física, Universidade Federal de São Carlos, São Paulo, Brazil, [3]Department of Chemistry and Center of NanoScience (CeNS), Ludwig-Maximilians-Universität, Munich, Germany

Since the obtaining of graphene, two-dimensional materials have emerged as a new class of nanomaterials with a plethora of new basic properties leading to a wide range of possible applications. In particular, 2D transition metal dichalcogenides (TMDs) and hexagonal boron nitride (h-BN) have been extensively studied due to their high nonlinear optical properties. In this review, we focused on the nonlinear properties of 2D nanomaterials covering the researches that explored their nonlinearities through optical imaging of the crystal structures.

KEYWORDS

nonlinear imaging, second-harmonic generation, four-wave mixing, transition metal dichalcogenides, hexagonal boron nitride, heterostructures

1 Introduction

Soon after the advent of the laser, nonlinear optical effects were experimentally demonstrated, in which the second harmonic generation (SHG) was the first phenomenon to be observed (Franken et al., 1961). Since then, many applications have been accomplished in a diversity of research and technology areas. For instance, nonlinear optical phenomena are the major source of new wavelength range pulses obtained from changing the frequency of pulsed femtosecond laser by interactions with nonlinear materials (Manzoni and Cerullo, 2016). In the last two decades, the development of user-friendly tabletop femtosecond Ti:Sapphire laser systems has led to the implementation of nonlinear optical microscopy by point scanning the pulsed laser beam over a material area and measuring the intensity map of the generated nonlinear signal. Nonlinear microscopy by harmonic generation, especially the second and the third harmonic generation (SHG and THG), four-wave mixing (FWM) and fluorescence by two-photon excitation (2PEF) have allowed to optically obtain the structural characterization of 2D materials (Malard et al., 2013; Oliveira et al., 2015) and biological materials (Zipfel et al., 2003; Ouellette et al., 2021; Cunha et al., 2021; Gomes et al., 2023). The overwhelming amount of publications on nonlinear properties of 2D nanomaterials make it hard to provide a comprehensive review of the literature. Thus, in this mini-review, we present and discuss how different nonlinear imaging techniques was employed to investigate and characterize 2D materials. The discussion is separated into sections of second and third-order nonlinear optical imaging.

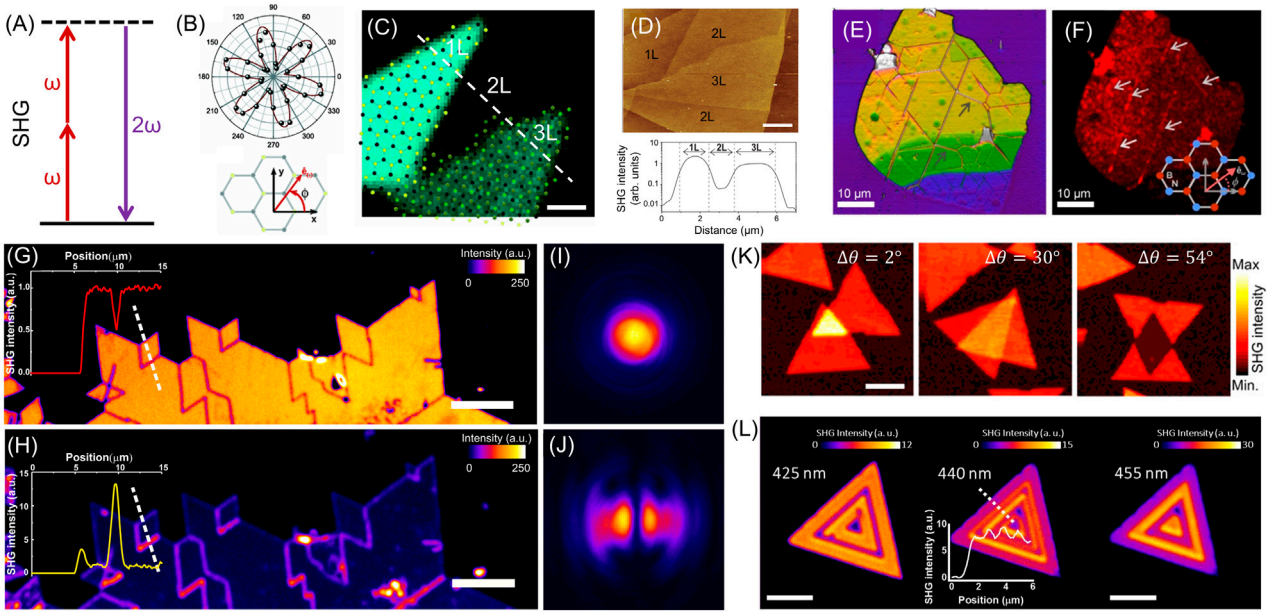

FIGURE 1
SHG Imaging: **(A)** SHG energy level diagram representing two photons of frequency ω generating one photon of frequency 2ω. **(B)** Polar plot of the SH intensity from a MoS_2 monolayer as a function of the sample angle exhibiting a six-fold pattern. At the bottom of **(B)**, the sample axes are indicated in the top view of the MoS_2 crystallographic orientation with respect to the incident laser polarization ($\hat{e}_\omega$). **(C)** SHG image showing the crystallographic orientation for a monolayer and trilayer MoS_2 sample determined by the polarization measurements, scale bar 5 μm. Brighter colors mean stronger SHG intensity. **(D)** AFM image (top map), scale bar 1 μm, and SH intensity profile (bottom graph) of the MoS_2 sample shown in **(C)** highlighting the quenched SH signal at even-layered TMDs in contrast to the strong SH emission of odd-layered TMDs. The SH intensity profile was taken along the dashed white line displayed in **(C)**. **(B–D)** Modified with permission from ref. (Malard et al., 2013). **(E)** AFM and **(F)** SHG images of a h-BN flake revealing wrinkles over the sample. Brighter colors indicate stronger SHG intensity. **(E, F)** Reprinted with permission from ref. (Oliveira et al., 2015). **(G)** Bright-field and **(H)** dark-field SHG imaging of a $MoSe_2$ monolayer showing quenched and enhanced SH signals, respectively, at edges and grain boundaries, scale bars 10 μm. **(I, J)** Spatial mode of the SH signal from a grain **(I)** and grain boundary **(J)** of a $MoSe_2$ monolayer underlining the dependence of the SH interference on the emitting angle at grain boundaries. **(G–J)** Reprinted with permission from ref. (Carvalho et al., 2019). Copyright 2020 American Chemical Society. **(K)** SHG imaging of twisted MoS_2 bilayers presenting the twist angle dependent SH interference, in which $\Delta\theta \approx 0$ lead to a constructive interference while $\Delta\theta \approx 60$ induce destructive interference, scale bar 5 μm. **(K)** Reprinted with permission from ref. (Hsu et al., 2014). Copyright 2014 American Chemical Society. **(L)** SHG imaging os a monolayer $WSe_2/MoSe_2$ lateral heterostructure displaying an enhanced signal the sharp heterojunctions. Due to excitonic resonant effects, the SH response from each monolayer is modulated by varying the emitting wavelength, scale bars 5 μm. **(L)** Reprinted with permission from ref. (Sousa et al., 2021).

2 Second-order nonlinear imaging

The continuous unveiling of novel properties in 2D materials with great appeal for future technologies is followed by a significant effort to improve growth techniques to provide large-area flakes in a scalable production (Zhang et al., 2019; Aras et al., 2022). Hence, methods to rapidly and easily characterize the crystal quality of these grown samples can highly contribute to developing the synthesis of 2D materials. In particular, synthesized large-area flakes ordinarily exhibit polycrystalline domains (Lin et al., 2016), highlighting the necessity of mapping the crystallographic orientation over the sample. For instance, transmission electron microscopy (TEM) measurements precisely determine the sample's crystallographic orientation (Huang et al., 2011; Yu et al., 2011; Ly et al., 2014). However, the mandatory use of a TEM grid and the limited measured area make such an experiment time-consuming, hampering its broad use. The SHG, which is a second-order nonlinear optical effect in which two incident fields with the same frequency ω generate a third field with frequency 2ω (see Figure 1A), is also sensitive to the crystalline properties of a material, enabling the ascertainment of its orientation (Malard et al., 2013; Li et al., 2013). Hence, as the SHG is a non-invasive technique that can be carried out for samples in standard substrates and can rapidly provide images over large areas, it has been extensively used for identifying crystallographic orientation. The first results were obtained for a few layers MoS_2 samples (Malard et al., 2013) where it has been shown that polarization-resolved SHG measurements provide crystallographic information of MoS_2 monolayer and trilayer exfoliated flakes, Figures 1B–D. Figure 1B shows a six-fold pattern of the SH intensity plotted as a function of the sample rotation angle, where the sketch indicates a top view showing the angle of the MoS_2 crystallographic orientation regarding the incident laser polarization direction ($\hat{e}_\omega$). Figure 1C shows SH images for the monolayer and trilayer MoS_2 samples together with the crystallographic orientation of the crystal lattice obtained from the polarization data. The AFM image of the sample indicating the number of layers and a SH intensity profile taken along the flakes are shown in Figure 1D. Note that due to the symmetry dependence, the SH signal is observed only for the odd layer positions in the sample (the $\chi^{(2)} = 0$ for the even layers). The difference in intensity observed for the monolayer and trilayer is due to resonance effects with the excitonic transitions (Malard et al., 2013). The crystallographic orientation is obtained by describing the electric field of the generated SH light (E (2ω)) along a given

direction ($\hat{e}_{2\omega}$) in terms of the second-order susceptibility tensor ($\chi^{(2)}$) and input light polarization vector ($\hat{e}_{\omega}$) as (Boyd, 2008; Shen, 2003):

$$\mathbf{E}(2\omega)\cdot\hat{e}_{2\omega} = C\hat{e}_{2\omega}\cdot\chi^{(2)}\colon \hat{e}_{\omega}\hat{e}_{\omega} \tag{1}$$

where ω is the laser frequency, 2ω is the SH frequency and C is a proportionality constant that contains local field factors determined by the local dielectric environment. Equation 1 describes the polarization dependence of the SHG and its specific form will depend on the $\chi^{(2)}$ tensor. For the TMDs, such as MoS_2, the odd-layered samples have D_{3h} point group symmetry, resulting in a second-order susceptibility tensor with a single non-zero element (Boyd, 2008; Shen, 2003): $\chi^{(2)}_{MoS_2} \equiv \chi^{(2)}_{xxx} = -\chi^{(2)}_{xyy} = -\chi^{(2)}_{yyx} = -\chi^{(2)}_{yxy}$, where x corresponds to the armchair direction since it has a mirror plane symmetry (Boyd, 2008; Shen, 2003), and y is the zigzag direction, as indicated in Figure 1B. Thus, the generated SH electric field as a function of the sample angle for a pump laser polarization ($\hat{e}_{\omega}$) parallel to the analyzer ($\hat{e}_{2\omega}$), is (Boyd, 2008; Shen, 2003):

$$E(2\omega) = C\chi^{(2)}_{MoS_2}\cos(3\phi + \phi_0) \tag{2}$$

where ϕ is the angle between the input laser polarization and the x direction, and ϕ_0 is the initial crystallographic orientation of MoS_2 sample. As the SH intensity is phase insensitive, there is an arbitrariness of $\pi/3$ in the definition of the x-axis.

Due to the sensitivity of SHG to the material's crystalline properties, one-dimensional defects such as edges, grain boundaries, and wrinkles are examples of common features presented by 2D materials that can be probed by SHG imaging (Oliveira et al., 2015; Yin et al., 2014; Karvonen et al., 2017; Carvalho et al., 2019). For instance, polarization-dependent SHG results have shown the formation of crystallographically-oriented origami-type wrinkles in annealed hexagonal boron nitride (h-BN) layers (Oliveira et al., 2015), Figures 1E, F. Additionally, Cunha et al. (2020) revealed the important role of defects in the increased efficiency of the SHG in h-BN flakes. SHG has also been used to reveal the crystalline details of grain boundaries. While the single crystalline grains exhibit uniform SHG intensities, edges and grain boundaries present a suppressed SH emission due to their translational symmetry breaking, which results in destructive interference of the SH fields and allows rapid visualization of these defective regions (Yin et al., 2014). Dark-field SHG imaging can also probe edges and grain boundaries in TMD monolayers (Carvalho et al., 2019). This method consists of blocking the central spot of the SH signal to collect only the emission at high angles, leading to an enhanced SH intensity at edges and grain boundaries, as displayed in Figures 1G–J. While there is destructive interference of the SH fields at small angles for these defective regions, large angles compensate for the fields' phase difference and result in constructive interference of the SHG at grain boundaries and edges (Carvalho et al., 2019). These angle-dependent constructive and destructive interferences are confirmed by the spatial mode of the SH emission of a $MoSe_2$ monolayer (Carvalho et al., 2019), as shown in Figures 1G, H. Additionally, grain boundaries of TMD monolayers can also be imaged by polarized SHG experiments (Van Der Zande et al., 2013; Cheng et al., 2015; David et al., 2015; Karvonen et al., 2017; Rosa et al., 2022; Sousa et al., 2024b). As the polarized SH intensity of these materials depends on the crystallographic orientation (Malard et al., 2013), grains with distinct orientations might display different polarized SH intensities, highlighting the boundaries between them (Van Der Zande et al., 2013; Cheng et al., 2015; David et al., 2015; Karvonen et al., 2017; Psilodimitrakopoulos et al., 2018; Rosa et al., 2022; Sousa et al., 2024b). Nonetheless, it is worth underlining that while TMD monolayers present a three-fold rotational symmetry, their polarized SHG exhibits a six-fold pattern, resulting in similar SH emissions for grains with anti-parallel crystallographic orientation.

In addition to the rich information directly given by the SHG imaging, it is also possible to employ data processing of the measured images to map distinct properties of the sample. For instance, a map of the crystallographic orientations of a TMD monolayer can be generated from polarization-resolved SHG imaging by fitting the angle-dependent SH expression (Equation 2) to the SH data of each measured pixel (David et al., 2015; Psilodimitrakopoulos et al., 2018). Besides, it was also reported a strain mapping of a TMD monolayer from polarization-resolved SHG imaging (Mennel et al., 2018; Li et al., 2019). As strain breaks the crystal symmetry of the material, it induces asymmetric intensities in the polarized SH six-fold pattern due to modifications in the second-order susceptibility tensor (Liang et al., 2017; Mennel et al., 2018; Mennel et al., 2019); Li et al., 2019). Hence, a photoelastic tensor was introduced to account for the role of the strain tensor on the nonlinear susceptibility tensor, allowing the evaluation of the strain field on the sample from polarization-resolved SHG measurements (Mennel et al., 2018; Mennel et al., 2019). Therefore, strain fields over a TMD monolayer can be mapped using this approach for each measured pixel of the polarized SHG images (Mennel et al., 2018).

Exploring the 2D materials field, we find that enormous efforts are also being placed in producing and investigating 2D heterostructures (Geim and Grigorieva, 2013; Novoselov et al., 2016; Castellanos-Gomez et al., 2022). For vertically stacked 2D materials, for example, novel and promising physical phenomena were revealed to be highly dependent on the twist angle between the forming layers (Castellanos-Gomez et al., 2022). Hence, SHG imaging emerges as a powerful non-invasive technique to determine the relative orientation between layers in 2D TMD heterostructures as well. This crystallographic orientation monitoring is simpler when the fabricated vertical heterostructure presents individual monolayers with non-overlapping areas (Hsu et al., 2014; Kim et al., 2021; Yuan et al., 2023). In such cases, it is possible to determine the crystallographic orientation of each monolayer from their isolated regions. However, as mentioned before, samples with θ or $\pi/3-\theta$ crystallographic orientations might exhibit the same polarized SH response, thus the SH signal from the heterostructure should also be analyzed to ascertain the monolayers' relative orientation (Hsu et al., 2014; Psilodimitrakopoulos et al., 2020; Kim et al., 2021; Yuan et al., 2023; Palekar et al., 2024). The SH emission of a twisted TMD bilayer, for example, is the coherent superposition of the SH emission from each monolayer, in which the bilayer SH intensity (I_T) is given by $I_T = I_1 + I_2 + 2\sqrt{I_1 I_2}\cos(3(\theta_1 - \theta_2))$, with I_1 and I_2 the SH intensities from the individual monolayers and θ_1 and θ_2 their orientations (Hsu et al., 2014). Therefore, $\Delta\theta$ and $\pi/3-\Delta\theta$ relative orientations can be differentiated from the type of SH interference presented at the twisted bilayer region (Hsu et al., 2014), as displayed in Figure 1K.

Twist angle analysis through SHG imaging experiments is not straightforward when the heterostructure contains monolayers without isolated regions. For a twisted TMD homobilayer in which one monolayer presents an isolated region and the other is entirely overlapped, it is elementary to obtain I_1, θ_1, and I_T. Since it is a homobilayer, it is expected that $I_1 = I_2$; thus θ_2 and the twist angle can be determined (Psilodimitrakopoulos et al., 2019; Xu et al., 2024). Note, however, that this approach cannot be applied to heterobilayers. In turn, the crystallographic orientations of the forming monolayers of an entirely overlapped TMD heterobilayer can be ascertained using polarization-resolved resonant SH imaging (Paradisanos et al., 2022). When one of the virtual states of the SHG process is in resonance with a real electronic or excitonic state, the SH intensity is highly increased (Malard et al., 2013; Wang et al., 2015b; Seyler et al., 2015; Wang et al., 2015a; Zhao et al., 2016; Lafeta et al., 2021; Shree et al., 2021; Sousa et al., 2024c). Thereby, if the excitation energy (or twice the excitation energy) is in resonance with an excitonic state of one of the TMD monolayers of the twisted bilayer, the SH emission of the heterostructure will be dominated by the signal from this specific monolayer and its crystallographic orientation can be accessed (Paradisanos et al., 2022). The twist angle of a TMD heterobilayer can be determined thus by performing polarization-resolved SHG imaging in resonance with each monolayer (Paradisanos et al., 2022). A real-time measurement of the stacking angle in a TMD heterobilayer was also reported by imaging two orthogonal components of the SH signal directly on the monolayers' overlapped region (Psilodimitrakopoulos et al., 2020), as $\Delta\theta$ can be written as a function of these perpendicular quantities from the interference SHG equation. Beyond the vertical heterostructures, SHG imaging has also been employed to probe coherent superposition effects in TMD lateral heterostructures (Sousa et al., 2021). The reported enhanced SH emission at the sharp TMD lateral heterojunctions due to a constructive interference revealed the capability of SHG imaging to probe these sharp interfaces (Sousa et al., 2021), as shown in Figure 1L. Moreover, such an experiment also allows the exploration of phase differences arising from the distinct second-order susceptibilities between the TMD monolayers (Kim et al., 2020; Sousa et al., 2021).

Also regarding 2D heterostructures, it has been recently demonstrated that the stacking of TMD monolayers can be used to boost the nonlinear optical gain and reach strong SHG signals (Trovatello et al., 2021), achieving optical parametric amplification in 2D TMDs. Furthermore, high nonlinear conversion efficiencies were obtained by controlling the phase-matching in multilayer 3R-MoS_2 with large thickness (Xu et al., 2022). Finally, SHG imaging was also employed to directly probe an incommensurate to commensurate phase transition in graphene/h-BN vertical heterostructures (Stepanov et al., 2020). While the centrosymmetric character of graphene is not affected by the h-BN bottom layer for an incommensurate alignment, the transition to a commensurate phase results in the breaking of graphene inversion symmetry and thus a finite SH emission (Stepanov et al., 2020).

TMD monolayers also exhibit singular valley phenomena (Xiao et al., 2012; Mak et al., 2012; Cao et al., 2012; Sousa et al., 2024a) due to their strong spin-orbit coupling and broken inversion symmetry, leading to a spin-valley locking effect at the inequivalent K and K′ valleys. This coupling between spin and valley degrees of freedom, which can be selectively accessed by circularly polarized light (Mak et al., 2012; Cao et al., 2012), sheds light on a novel field with promising potential for data storage, manipulation, and readout named valleytronics (Schaibley et al., 2016). Hence, control over valley polarization is essential in view of technological applications, resulting in a demand for methods to probe valley asymmetries in 2D materials. In this sense, a SHG imaging technique was recently used to map the valley imbalance in TMD monolayers (Mouchliadis et al., 2021). A valley polarization out of equilibrium impacts the crystal symmetry, thus inducing new terms in the material's second-order susceptibility tensor and modifying the SH emission (Hipolito and Pereira, 2017). Particularly, the intrinsic ($\chi^{(2)}_{\text{int}}$) and valley-polarization-induced ($\chi^{(2)}_{\text{vp}}$) second-order susceptibility terms for TMD monolayers lead to orthogonal SHG polarizations, resulting in a rotation of the polarized SH six-fold pattern dependent on the valley imbalance (Ho et al., 2020; Mouchliadis et al., 2021; Herrmann et al., 2023). Therefore, by using an elliptical polarized excitation and detecting the polarization-resolved SH emission, it is possible to create a valley imbalance in TMD monolayers and indirectly track it through the rotation of the polarized SH pattern (Ho et al., 2020; Mouchliadis et al., 2021; Herrmann et al., 2023). As valley imbalance is mainly generated by a valley-polarized exciton population in TMD monolayers, resonant excitation also plays a major role in this phenomenon (Ho et al., 2020). However, it is worth stressing that further effects such as valley-exclusive optical Stark or Bloch-Siegert shifts can also induce valley polarization by breaking the time-reversal symmetry in TMD monolayers (Sie et al., 2017), which was demonstrated through SHG as well (Herrmann et al., 2023). Notably, these valley asymmetries in TMD monolayers are widely investigated by circularly polarized photoluminescence and absorption experiments (Mak et al., 2012; Cao et al., 2012). Nonetheless, these measurements cannot be used for gapless materials such as graphene, which also present valley phenomena (Rycerz et al., 2007; Xiao et al., 2007; Yao et al., 2008). In contrast, it is possible to measure valley population imbalances even in centrosymmetric crystals as graphene (Golub and Tarasenko, 2014), since this valley asymmetry lowers the crystal symmetry leading to non-zero terms in its second-order susceptibility.

Beyond the largely investigated 2D materials like graphene, h-BN, and TMDs, SHG has also been employed to probe magnetic symmetries in emergent layered magnets such as CrI_3, CrSBr, and $MnPS_3$ (Wu et al., 2024). Although these materials are centrosymmetric in the paramagnetic phase, their antiferromagnetic ordering leads to an inversion symmetry breaking. Hence, an enhancement of the SH emission is observed below the Néel temperature, providing an all-optical and rapid method to probe magnetic phase transitions in these materials (Sun et al., 2019; Chu et al., 2020; Lee et al., 2021). In particular, SHG imaging was used to map this magnetic phase transition on a CrI_3 bilayer (Sun et al., 2019).

Despite the standard polarized SHG techniques presented above as consolidated and powerful tools to determine the orientation and symmetry properties of 2D materials, other innovative approaches using SHG improved and extended this second-order nonlinear technique to determine other properties and explore different materials. An example of this recent development is the Fourier space SH imaging, which provides a straightforward method to determine the crystallographic orientation and symmetry based on

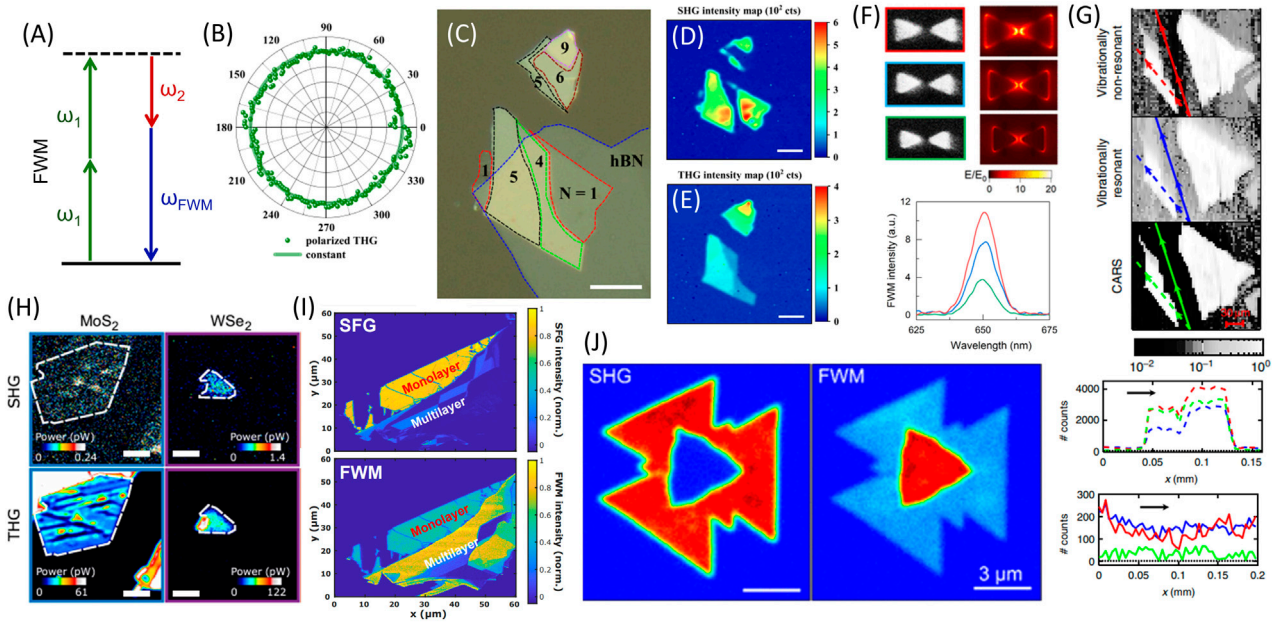

FIGURE 2
FWM Imaging: **(A)** Energy diagram of degenerate four-wave mixing process. **(B)** Polar plot of the third harmonic intensity from WSe_2 as a function of the sample angle. **(C)** Optical image of the sample with the labeled number of layers (N), scale bar 10 μm. **(D, E)** Spatial SHG and THG intensity mappings across the WSe_2 sample, scale bars 10 μm. **(B–E)** Reprinted with permission from ref. (Rosa et al., 2018). **(F)** FWM enhancement with different plasmonic structure dimensions; top, the scanning electron microscopy (SEM) images and the simulated electric field at 800 nm of Au bowtie structures with different sizes (s = 160, 140, and 120 nm); bottom, the experimental FWM spectra of the corresponding MoS_2-plasmonic structures. **(F)** Reprinted with permission from ref. (Dai et al., 2021). **(G)** Top, nonlinear optical images of few-layer graphene (FLG) measured under a nonvibrationally resonant λ_S at 891.5 nm (red lines), resonant λ_S at 894 nm (blue lines) and ΔT = 1.7 ps and CARS image of two FLG flakes, obtained by the spectral dip (green lines). Bottom, intensity profiles along the scanning paths in and out of a FLG flake as highlighted in the images on top by dashed and full lines, respectively. **(G)** Reprinted with permission from ref. (Virga et al., 2019). **(H)** SHG (top) and THG (bottom) images from MoS_2 and WSe_2 samples, scale bars 10 μm. **(H)** Reprinted with permission from ref. (Autere et al., 2018). **(I)** Sum-frequency generation (top) and FWM (bottom) intensity images of a WSe_2 sample extracted from Supporting information of ref. (Lange et al., 2024). Copyright 2024 American Chemical Society. **(J)** SHG (left) and FWM (right) of a synthesized MoS_2 sample. **(J)** Reprinted with permission from ref. (Balla et al., 2018). Copyright 2018 American Chemical Society.

the images generated by the SH signal in Fourier space using an azimuthal laser mode to excite the sample (Lafeta et al., 2025). In addition, there is also a great interest in developing the potential of SHG techniques to improve their spatial resolution. Although considerable efforts are employed to achieve increased spatial resolutions for SHG imaging (Psilodimitrakopoulos et al., 2018), there is the intrinsic confocal optics resolution limitation of hundreds of nm due to the diffraction limit of light. Therefore, nonlinear near-field techniques emerge as a powerful alternative for imaging the nanoscale SH responses (Yao et al., 2022; Luo et al., 2023). For example, localized variations of the stacking order in a TMD homobilayer as well as excitonic resonances were recently probed by nano-SHG imaging with a spatial resolution down to 20 nm (Yao et al., 2022). Moreover, nano-SHG imaging could also detect localized variations in the symmetry of a TMD monolayer (Luo et al., 2023).

3 Third-order nonlinear imaging

Similar to second-order optical effects, third-order nonlinear processes play an important role and significantly contribute to the study of 2D materials. The general third-order nonlinear optical phenomenon is known as four-wave mixing (FWM), which depends on the third-order electrical susceptibility ($\chi^{(3)}$) and can be generated by any combination of three electric fields of frequencies ω_1, ω_2, and ω_3 generating a fourth one of frequency $\omega_{FWM} = |\pm \omega_1 \pm \omega_2 \pm \omega_3|$ in a nonlinear medium. This phenomenon has exciting applications in 2D materials, mainly because it could be applied to centrosymmetric materials, contrasting with second-order nonlinear processes limited to noncentrosymmetric materials (Boyd, 2008). The FWM presents some important particular cases, such as the degenerated four-wave mixing (DFWM), in which two of the incident fields are frequency degenerate, for example, $\omega_1 = \omega_3$, resulting in $\omega_{DFWM} = 2\omega_1 - \omega_2$ (see Figure 2A) (Lafeta et al., 2021). Another special case commonly exploited in the 2D materials investigation is the third harmonic generation (THG), which occurs when the three incident fields have the same frequency ($\omega_1 = \omega_2 = \omega_3$); thus $\omega_{THG} = 3\omega_1$ (Wen et al., 2019).

Previous studies have explored the dependence of polarization in exceptional cases of FWM. In particular, Wang et al. (2014); Woodward et al. (2016) investigated the polarization dependence of THG, showing that third-harmonic signals from D_{3h} symmetry materials align with the polarization of the three incident fields when they share the same linear polarization. This result was reproduced by Rosa et al. (2018), as illustrated in Figure 2B. The polarization dependence of DFWM, which exhibits additional

degrees of freedom compared to THG, has also been reported for D_{3h} symmetry materials. Li et al. (2016) examined DFWM signals for three polarization configurations: rotating only ω_1 incident field, rotating only ω_2 field, and rotating both ω_1 and ω_2 fields. However, they noted that when the experiments rotated the ω_2 field, the results were inconclusive due to the broadband nature of the ω_2 beam they used. Later, Balla et al. (2018) showed that when the polarizations of both incident beams are parallel and rotated with a fixed analyzer, the DFWM signal behaves like THG, aligning with the polarization of the incident fields. Dai et al. (2021) corroborated this, using lasers with parallel and fixed polarizations and rotating a polarizer in front of the detector. Furthermore, Dai et al. (2021) reproduced the first condition presented by Li et al. (2016) rotating ω_1 with ω_2 fixed, indicating that the rotation of the broadband ω_2 beams probably caused earlier inconsistencies. Dai et al. (2021) further demonstrated enhanced DFWM signals using hybrid MoS_2-plasmonic structures of varying sizes, as shown in Figure 2F. They also examined DFWM polarization dependence by rotating both incident beams in pristine and hybrid MoS_2-plasmonic structures. Maximum signals were observed when incident fields were aligned parallel to the longitudinal direction of the cavity.

In general, TMDs present a strong FWM signal that increases with the number of layers (Li et al., 2016; Säynätjoki et al., 2017; Rosa et al., 2018; Autere et al., 2018; Balla et al., 2018; Lange et al., 2024), as shown in Figures 2C–E, H–J. This FWM response complements the second-order techniques that cannot probe centrosymmetric materials such as even-layered TMDs due to their D_{3d} symmetry (Malard et al., 2013; Li et al., 2013). Furthermore, resonances with excitons were also observed by FWM experiments when incident fields lead to a ω_{FWM} that matches the excitons frequency in TMDs (Lafeta et al., 2021), demonstrating the potential of this technique to characterize, for example, the impact of doping on the excitonic responses of TMD materials (Sousa et al., 2024a; Sousa et al., 2024c). Bauer et al. (2022) also studied the effect of excitonic resonances on the dynamics of second- and third-order effects on 2D TMDs, revealing that temporal delays between incident fields can be required to maximize the resonant nonlinear optical responses of TMDs. Besides, Karvonen et al. (2017) used THG imaging to investigate grain boundaries in synthesized MoS_2 monolayers, showing an enhanced contrast of this one-dimensional defect compared with SHG imaging; thus enabling its rapid visualization.

Moreover, FWM techniques using broadband lasers were also used to investigate TMDs. This method employs broadband incident laser pulses to generate a combination of third-order nonlinear responses over a large range of frequencies, which enables the investigation of several effects such as resonances with excitons in one single measurement (Ko et al., 2019) and the increase in the nonlinear signal produced by the control of the phase of the incident fields (Lange et al., 2024).

FWM imaging has also been employed to study other 2D materials such as graphene and h-BN, with a special interest in monolayer graphene because of its inversion symmetry and consequent absent SHG signal (Shan et al., 2018). Such investigations in these materials exploit a particular case of DFWM called coherent anti-Stokes Raman scattering (CARS), which occurs when the energy difference of the incident fields (ω_1 and ω_2) is equal to the energy of a vibrational mode (ω_Ω) of the material, i.e., $\omega_\Omega = \omega_1 - \omega_2$. This condition is a special type of stimulated Raman process that amplifies the anti-Stokes signal (Cheng and Xie, 2004). The CARS technique provided remarkable results in the studies of biological materials and more recently in carbon nanotubes (Duncan et al., 1982; Cheng and Xie, 2004; Potma and Xie, 2004; Polli et al., 2018; Li et al., 2020; Cunha et al., 2021; Paddubskaya et al., 2020; Gordeev et al., 2023). Since CARS is a label-free technique that uses just the Raman fingerprints as a marker, several works explore such experiments in biological applications. Nevertheless, CARS is also used to study 2D materials (Malard et al., 2021). For instance, an anomalous nonlinear behavior was reported for graphene when the DFWM satisfies the resonant CARS condition. Lafeta et al. (2017) showed an expected strong enhancement in the h-BN DFWM signal at the CARS resonance, while a decreased DFWM intensity at the CARS condition was observed for graphene, which was explained with a Fano resonance model (Fano, 1961). A posterior study confirmed this anomalous behavior and exploited the impact of applying a temporal delay between ω_1 and ω_2 incident fields, unveiling the temporal dynamics between the electronic transition and the vibrational resonant lifetimes (Virga et al., 2019), as shown in Figure 2G. Another work involving FWM and stimulated Raman scattering (SRS) imaging demonstrated the capacity of the latter to remove the nonresonant background in contrast to CARS in h-BN samples (Ling et al., 2019).

4 Conclusion and future perspectives

In this mini-review, we explored the progress of nonlinear optical imaging techniques for the study of nonlinear responses in 2D materials, focusing on second-order, specifically SHG, and third-order, FWM and its special cases. In particular, we discussed the potential of SHG experiments to probe symmetry information of h-BN and odd-layered TMD samples. This capability of SHG measurements to image the crystallographic orientations of these materials enables, for example, the study of one-dimensional defects such as wrinkles, edges, and grain boundaries, the determination of twist angles in 2D heterostructures, and the mapping of strain fields over the samples. Additionally, we discussed the importance of FWM experiments to investigate nonlinearities of centrosymmetric materials as graphene and even-layered TMDs, which present a negligible second-order nonlinear emission. Furthermore, we also addressed the potential of resonant SHG and FWM experiments to probe excitonic effects in TMDs. In summary, we highlighted that these non-invasive nonlinear techniques are powerful tools for the rapid imaging of 2D material properties, paving the way for the development of sample fabrication and the research of fundamental aspects of nonlinear optics. Moreover, we shed light on different possibilities to increase the potential of nonlinear imaging. For instance, the recent use of near-field SHG and FWM experiments allows the imaging of 2D materials with nanometric resolution, while the constant developments in nonlinear optics theory and data analysis enable to unveil notable properties as valley population imbalance in these samples.

Author contributions

FS: Investigation, Writing–original draft, Writing–review and editing. LL: Investigation, Writing–original draft, Writing–review and editing. GF: Investigation, Writing–original draft, Writing–review and editing. AdP: Conceptualization, Funding acquisition, Investigation, Writing–original draft, Writing–review and editing.

Funding

The author(s) declare that financial support was received for the research, authorship, and/or publication of this article. This work was financially supported by the Brazilian agencies Conselho Nacional de Desenvolvimento Científico e Tecnológico (CNPq), Fundação de Amparo à Pesquisa do Estado de Minas Gerais (Fapemig), Coordenação de Aperfeiçoamento de Pessoal de Nível Superior (Capes) and Institute of Science and Technology (INCT) in Carbon Nanomaterials. LL gratefully acknowledges the Alexander von Humboldt Foundation for its financial support.

Conflict of interest

The authors declare that the research was conducted in the absence of any commercial or financial relationships that could be construed as a potential conflict of interest.

Generative AI statement

The author(s) declare that no Generative AI was used in the creation of this manuscript.

Publisher's note

References

Aras, F. G., Yilmaz, A., Tasdelen, H. G., Ozden, A., Ay, F., Perkgoz, N. K., et al. (2022). A review on recent advances of chemical vapor deposition technique for monolayer transition metal dichalcogenides (MX2: Mo, W; S, Se, Te). *Mater. Sci. Semicond. Process.* 148, 106829. doi:10.1016/j.mssp.2022.106829

Autere, A., Jussila, H., Marini, A., Saavedra, J. R. M., Dai, Y., Säynätjoki, A., et al. (2018). Optical harmonic generation in monolayer group-VI transition metal dichalcogenides. *Phys. Rev. B* 98, 115426. doi:10.1103/PhysRevB.98.115426

Balla, N. K., O'Brien, M., McEvoy, N., Duesberg, G. S., Rigneault, H., Brasselet, S., et al. (2018). Effects of excitonic resonance on second and third order nonlinear scattering from few-layer mos2. *ACS Photonics* 5, 1235–1240. doi:10.1021/acsphotonics.7b00912

Bauer, J. M., Chen, L., Wilhelm, P., Watanabe, K., Taniguchi, T., Bange, S., et al. (2022). Excitonic resonances control the temporal dynamics of nonlinear optical wave mixing in monolayer semiconductors. *Nat. Photonics* 16, 777–783. doi:10.1038/s41566-022-01080-1

Boyd, R. (2008). *Nonlinear optics*. London: Academic Press.

Cao, T., Wang, G., Han, W., Ye, H., Zhu, C., Shi, J., et al. (2012). Valley-selective circular dichroism of monolayer molybdenum disulphide. *Nat. Commun.* 3, 887. doi:10.1038/ncomms1882

Carvalho, B. R., Wang, Y., Fujisawa, K., Zhang, T., Kahn, E., Bilgin, I., et al. (2019). Nonlinear dark-field imaging of one-dimensional defects in monolayer dichalcogenides. *Nano Lett.* 20, 284–291. doi:10.1021/acs.nanolett.9b03795

Castellanos-Gomez, A., Duan, X., Fei, Z., Gutierrez, H. R., Huang, Y., Huang, X., et al. (2022). Van der Waals heterostructures. *Nat. Rev. Methods Prim.* 2, 58. doi:10.1038/s43586-022-00139-1

Cheng, J., Jiang, T., Ji, Q., Zhang, Y., Li, Z., Shan, Y., et al. (2015). Kinetic nature of grain boundary formation in as-grown MoS_2 monolayers. *Adv. Mater. Deerf. Beach, Fla* 27, 4069–4074. doi:10.1002/adma.201501354

Cheng, J.-X., and Xie, X. S. (2004). Coherent anti-Stokes Raman scattering Microscopy: instrumentation, theory, and applications. *J. Phys. Chem. B* 108, 827–840. doi:10.1021/jp035693v

Chu, H., Roh, C. J., Island, J. O., Li, C., Lee, S., Chen, J., et al. (2020). Linear magnetoelectric phase in ultrathin mnps 3 probed by optical second harmonic generation. *Phys. Rev. Lett.* 124, 027601. doi:10.1103/physrevlett.124.027601

Cunha, R., Cadore, A., Ramos, S. L., Watanabe, K., Taniguchi, T., Kim, S., et al. (2020). Second harmonic generation in defective hexagonal boron nitride. *J. Phys. Condens. Matter* 32, 19LT01. doi:10.1088/1361-648x/ab6cbf

Cunha, R., Lafeta, L., Fonseca, E. A., Barbosa, A., Romano-Silva, M. A., Vieira, R., et al. (2021). Nonlinear and vibrational microscopy for label-free characterization of amyloid-β plaques in Alzheimer's disease model. *Analyst* 146, 2945–2954. doi:10.1039/D1AN00074H

Dai, Y., Wang, Y., Das, S., Li, S., Xue, H., Mohsen, A., et al. (2021). Broadband plasmon-enhanced four-wave mixing in monolayer MoS_2. *Nano Lett.* 21, 6321–6327. doi:10.1021/acs.nanolett.1c02381

David, S. N., Zhai, Y., Van Der Zande, A. M., O'Brien, K., Huang, P. Y., Chenet, D. A., et al. (2015). Rapid, all-optical crystal orientation imaging of two-dimensional transition metal dichalcogenide monolayers. *Appl. Phys. Lett.* 107. doi:10.1063/1.4930232

Duncan, M. D., Reintjes, J., and Manuccia, T. J. (1982). Scanning coherent anti-Stokes Raman microscope. *Opt. Lett.* 7, 350–352. doi:10.1364/OL.7.000350

Fano, U. (1961). Effects of configuration interaction on intensities and phase shifts. *Phys. Rev.* 124, 1866–1878. doi:10.1103/PhysRev.124.1866

Franken, P. A., Hill, A. E., Peters, C. W., and Weinreich, G. (1961). Generation of optical harmonics. *Phys. Rev. Lett.* 7, 118–119. doi:10.1103/PhysRevLett.7.118

Geim, A. K., and Grigorieva, I. V. (2013). Van der Waals heterostructures. *Nature* 499, 419–425. doi:10.1038/nature12385

Golub, L., and Tarasenko, S. (2014). Valley polarization induced second harmonic generation in graphene. *Phys. Rev. B* 90, 201402. doi:10.1103/physrevb.90.201402

Gomes, E. F. A., Paulino Junior, E., de Lima, M. F. R., Reis, L. A., Paranhos, G., Mamede, M., et al. (2023). Prostate cancer tissue classification by multiphoton imaging, automated image analysis and machine learning. *J. Biophot.* 16, e202200382. doi:10.1002/jbio.202200382

Gordeev, G., Lafeta, L., Flavel, B. S., Jorio, A., and Malard, L. M. (2023). Excitonic resonances in coherent anti-Stokes Raman scattering from single-walled carbon nanotubes. *J. Phys. Chem. C* 127, 20438–20444. doi:10.1021/acs.jpcc.3c05696

Herrmann, P., Klimmer, S., Lettau, T., Monfared, M., Staude, I., Paradisanos, I., et al. (2023). Nonlinear all-optical coherent generation and read-out of valleys in atomically thin semiconductors. *Small* 19, 2301126. doi:10.1002/smll.202301126

Hipolito, F., and Pereira, V. M. (2017). Second harmonic spectroscopy to optically detect valley polarization in 2D materials. *2D Mater.* 4, 021027. doi:10.1088/2053-1583/aa6f4d

Ho, Y. W., Rosa, H. G., Verzhbitskiy, I., Rodrigues, M. J., Taniguchi, T., Watanabe, K., et al. (2020). Measuring valley polarization in two-dimensional materials with second-harmonic spectroscopy. *ACS Photonics* 7, 925–931. doi:10.1021/acsphotonics.0c00174

Hsu, W.-T., Zhao, Z.-A., Li, L.-J., Chen, C.-H., Chiu, M.-H., Chang, P.-S., et al. (2014). Second harmonic generation from artificially stacked transition metal dichalcogenide twisted bilayers. *ACS Nano* 8, 2951–2958. doi:10.1021/nn500228r

Huang, P. Y., Ruiz-Vargas, C. S., Van Der Zande, A. M., Whitney, W. S., Levendorf, M. P., Kevek, J. W., et al. (2011). Grains and grain boundaries in single-layer graphene atomic patchwork quilts. *Nature* 469, 389–392. doi:10.1038/nature09718

Karvonen, L., Säynätjoki, A., Huttunen, M. J., Autere, A., Amirsolaimani, B., Li, S., et al. (2017). Rapid visualization of grain boundaries in monolayer MoS2 by multiphoton microscopy. *Nat. Commun.* 8, 15714. doi:10.1038/ncomms15714

Kim, W., Ahn, J. Y., Oh, J., Shim, J. H., and Ryu, S. (2020). Second-harmonic young's interference in atom-thin heterocrystals. *Nano Lett.* 20, 8825–8831. doi:10.1021/acs.nanolett.0c03763

Kim, Y. C., Yoo, H., Nguyen, V. T., Lee, S., Park, J.-Y., and Ahn, Y. H. (2021). High-speed imaging of second-harmonic generation in MoS_2 bilayer under femtosecond laser ablation. *Nanomaterials* 11, 1786. doi:10.3390/nano11071786

Ko, B. A., Sokolov, A. V., Scully, M. O., Zhang, Z., and Lee, H. W. H. (2019). Enhanced four-wave mixing process near the excitonic resonances of bulk MoS_2. *Phot. Res.* 7, 251–259. doi:10.1364/PRJ.7.000251

Lafeta, L., Cadore, A. R., Mendes-de Sa, T. G., Watanabe, K., Taniguchi, T., Campos, L. C., et al. (2017). Anomalous nonlinear optical response of graphene near phonon resonances. *Nano Lett.* 17, 3447–3451. doi:10.1021/acs.nanolett.7b00329

Lafeta, L., Corradi, A., Zhang, T., Kahn, E., Bilgin, I., Carvalho, B. R., et al. (2021). Second- and third-order optical susceptibilities across excitons states in 2D monolayer transition metal dichalcogenides. *2D Mater.* 8, 035010. doi:10.1088/2053-1583/abeed4

Lafeta, L., Hartmann, S., Rosa, B., Reitzenstein, S., Malard, L. M., and Hartschuh, A. (2025). Probing noncentrosymmetric 2D materials by Fourier space second harmonic imaging. *ACS Photonics* 12, 357–363. doi:10.1021/acsphotonics.4c01724

Lange, L., Wang, K., Bange, S., Lafeta, L., Rosa, B., Reitzenstein, S., et al. (2024). Ultrafast phase-control of the nonlinear optical response of 2D semiconductors. *ACS Photonics* 11, 3112–3122. doi:10.1021/acsphotonics.4c00388

Lee, K., Dismukes, A. H., Telford, E. J., Wiscons, R. A., Wang, J., Xu, X., et al. (2021). Magnetic order and symmetry in the 2d semiconductor crsbr. *Nano Lett.* 21, 3511–3517. doi:10.1021/acs.nanolett.1c00219

Li, D., Wei, C., Song, J., Huang, X., Wang, F., Liu, K., et al. (2019). Anisotropic enhancement of second-harmonic generation in monolayer and bilayer MoS_2 by integrating with TiO_2 nanowires. *Nano Lett.* 19, 4195–4204. doi:10.1021/acs.nanolett.9b01933

Li, D., Xiong, W., Jiang, L., Xiao, Z., Rabiee Golgir, H., Wang, M., et al. (2016). Multimodal nonlinear optical imaging of mos2 and mos2-based van der waals heterostructures. *ACS Nano* 10, 3766–3775. doi:10.1021/acsnano.6b00371

Li, S., Li, Y., Yi, R., Liu, L., and Qu, J. (2020). Coherent anti-Stokes Raman scattering microscopy and its applications. *Front. Phys.* 8. doi:10.3389/fphy.2020.598420

Li, Y., Rao, Y., Mak, K. F., You, Y., Wang, S., Dean, C. R., et al. (2013). Probing symmetry properties of few-layer MoS_2 and h-BN by optical second-harmonic generation. *Nano Lett.* 13, 3329–3333. doi:10.1021/nl401561r

Liang, J., Zhang, J., Li, Z., Hong, H., Wang, J., Zhang, Z., et al. (2017). Monitoring local strain vector in atomic-layered $MoSe_2$ by second-harmonic generation. *Nano Lett.* 17, 7539–7543. doi:10.1021/acs.nanolett.7b03476

Lin, Z., Carvalho, B. R., Kahn, E., Lv, R., Rao, R., Terrones, H., et al. (2016). Defect engineering of two-dimensional transition metal dichalcogenides. *2D Mater.* 3, 022002. doi:10.1088/2053-1583/3/2/022002

Ling, J., Miao, X., Sun, Y., Feng, Y., Zhang, L., Sun, Z., et al. (2019). Vibrational imaging and quantification of two-dimensional hexagonal Boron Nitride with stimulated Raman scattering. *ACS Nano* 13, 14033–14040. doi:10.1021/acsnano.9b06337

Luo, W., Whetten, B. G., Kravtsov, V., Singh, A., Yang, Y., Huang, D., et al. (2023). Ultrafast nanoimaging of electronic coherence of monolayer WSe_2. *Nano Lett.* 23, 1767–1773. doi:10.1021/acs.nanolett.2c04536

Ly, T. H., Chiu, M.-H., Li, M.-Y., Zhao, J., Perello, D. J., Cichocka, M. O., et al. (2014). Observing grain boundaries in CVD-grown monolayer transition metal dichalcogenides. *ACS Nano* 8, 11401–11408. doi:10.1021/nn504470q

Mak, K. F., He, K., Shan, J., and Heinz, T. F. (2012). Control of valley polarization in monolayer MoS_2 by optical helicity. *Nat. Nanotechnol.* 7, 494–498. doi:10.1038/nnano.2012.96

Malard, L. M., Alencar, T. V., Barboza, A. P. M., Mak, K. F., and de Paula, A. M. (2013). Observation of intense second harmonic generation from atomic crystals. *Phys. Rev. B* 87, 201401. doi:10.1103/physrevb.87.201401

Malard, L. M., Lafeta, L., Cunha, R. S., Nadas, R., Gadelha, A., Cançado, L. G., et al. (2021). Studying 2D materials with advanced Raman spectroscopy: CARS, SRS and TERS. *Phys. Chem. Chem. Phys.* 23, 23428–23444. doi:10.1039/D1CP03240B

Manzoni, C., and Cerullo, G. (2016). Design criteria for ultrafast optical parametric amplifiers. *J. Opt.* 18, 103501. doi:10.1088/2040-8978/18/10/103501

Mennel, L., Furchi, M. M., Wachter, S., Paur, M., Polyushkin, D. K., and Mueller, T. (2018). Optical imaging of strain in two-dimensional crystals. *Nat. Commun.* 9, 516. doi:10.1038/s41467-018-02830-y

Mennel, L., Paur, M., and Mueller, T. (2019). Second harmonic generation in strained transition metal dichalcogenide monolayers: MoS_2, $MoSe_2$, WS_2, and WSe_2. *Apl. Photonics* 4, 034404. doi:10.1063/1.5051965

Mouchliadis, L., Psilodimitrakopoulos, S., Maragkakis, G. M., Demeridou, I., Kourmoulakis, G., Lemonis, A., et al. (2021). Probing valley population imbalance in transition metal dichalcogenides via temperature-dependent second harmonic generation imaging. *npj 2D Mater. Appl.* 5 (6), 6. doi:10.1038/s41699-020-00183-z

Novoselov, K. S., Mishchenko, A., Carvalho, A., and Castro Neto, A. (2016). 2d materials and van der Waals heterostructures. *Science* 353, aac9439. doi:10.1126/science.aac9439

Oliveira, C. K., Gomes, E. F. A., Prado, M. C., Alencar, T. V., Nascimento, R., Malard, L. M., et al. (2015). Crystal-oriented wrinkles with origami-type junctions in few-layer hexagonal boron nitride. *Nano Res.* 8, 1680–1688. doi:10.1007/s12274-014-0665-y

Ouellette, J. N., Drifka, C. R., Pointer, K. B., Liu, Y., Lieberthal, T. J., Kao, W. J., et al. (2021). Navigating the collagen jungle: the biomedical potential of fiber organization in cancer. *Bioengineering* 8, 17. doi:10.3390/bioengineering8020017

Paddubskaya, A., Rutkauskas, D., Karpicz, R., Dovbeshko, G., Nebogatikova, N., Antonova, I., et al. (2020). Recognition of spatial distribution of CNT and graphene in hybrid structure by mapping with coherent anti-Stokes Raman microscopy. *Nanoscale Res. Lett.* 15, 37. doi:10.1186/s11671-020-3264-8

Palekar, C. C., Faria Junior, P. E., Rosa, B., Sousa, F. B., Malard, L. M., Fabian, J., et al. (2024). Amplification of interlayer exciton emission in twisted WSe_2/WSe_2/$MoSe_2$ heterotrilayers. *npj 2D Mater. Appl.* 8, 49. doi:10.1038/s41699-024-00483-8

Paradisanos, I., Raven, A. M. S., Amand, T., Robert, C., Renucci, P., Watanabe, K., et al. (2022). Second harmonic generation control in twisted bilayers of transition metal dichalcogenides. *Phys. Rev. B* 105, 115420. doi:10.1103/physrevb.105.115420

Polli, D., Kumar, V., Valensise, C. M., Marangoni, M., and Cerullo, G. (2018). Broadband coherent Raman scattering microscopy. *Laser and Photonics Rev.* 12, 1800020. doi:10.1002/lpor.201800020

Potma, E. O., and Xie, X. S. (2004). Cars microscopy for biology and medicine. *Opt. Phot. News* 15, 40–45. doi:10.1364/OPN.15.11.000040

Psilodimitrakopoulos, S., Mouchliadis, L., Maragkakis, G. M., Kourmoulakis, G., Lemonis, A., Kioseoglou, G., et al. (2020). Real-time spatially resolved determination of twist angle in transition metal dichalcogenide heterobilayers. *2D Mater.* 8, 015015. doi:10.1088/2053-1583/abbf88

Psilodimitrakopoulos, S., Mouchliadis, L., Paradisanos, I., Kourmoulakis, G., Lemonis, A., Kioseoglou, G., et al. (2019). Twist angle mapping in layered WS2 by polarization-resolved second harmonic generation. *Sci. Rep.* 9, 14285. doi:10.1038/s41598-019-50534-0

Psilodimitrakopoulos, S., Mouchliadis, L., Paradisanos, I., Lemonis, A., Kioseoglou, G., and Stratakis, E. (2018). Ultrahigh-resolution nonlinear optical imaging of the armchair orientation in 2D transition metal dichalcogenides. *Light Sci. and Appl.* 7, 18005. doi:10.1038/lsa.2018.5

Rosa, B. L. T., Fujisawa, K., Santos, J. C. C., Zhang, T., Matos, M. J. S., Sousa, F. B., et al. (2022). Investigation of spatially localized defects in synthetic monolayers. *Phys. Rev. B* 106, 115301. doi:10.1103/PhysRevB.106.115301

Rosa, H. G., Ho, Y. W., Verzhbitskiy, I., Rodrigues, M. J. F. L., Taniguchi, T., Watanabe, K., et al. (2018). Characterization of the second- and third-harmonic optical susceptibilities of atomically thin tungsten diselenide. *Sci. Rep.* 8, 10035. doi:10.1038/s41598-018-28374-1

Rycerz, A., Tworzydło, J., and Beenakker, C. (2007). Valley filter and valley valve in graphene. *Nat. Phys.* 3, 172–175. doi:10.1038/nphys547

Säynätjoki, A., Karvonen, L., Rostami, H., Autere, A., Mehravar, S., Lombardo, A., et al. (2017). Ultra-strong nonlinear optical processes and trigonal warping in mos2 layers. *Nat. Commun.* 8, 893. doi:10.1038/s41467-017-00749-4

Schaibley, J. R., Yu, H., Clark, G., Rivera, P., Ross, J. S., Seyler, K. L., et al. (2016). Valleytronics in 2D materials. *Nat. Rev. Mater.* 1, 16055. doi:10.1038/natrevmats.2016.55

Seyler, K. L., Schaibley, J. R., Gong, P., Rivera, P., Jones, A. M., Wu, S., et al. (2015). Electrical control of second-harmonic generation in a WSe_2 monolayer transistor. *Nat. Nanotechnol.* 10, 407–411. doi:10.1038/nnano.2015.73

Shan, Y., Li, Y., Huang, D., Tong, Q., Yao, W., Liu, W.-T., et al. (2018). Stacking symmetry governed second harmonic generation in graphene trilayers. *Sci. Adv.* 4, eaat0074. doi:10.1126/sciadv.aat0074

Shen, Y. R. (2003). *The principles of nonlinear optics*. New York: Wiley Interscience.

Shree, S., Lagarde, D., Lombez, L., Robert, C., Balocchi, A., Watanabe, K., et al. (2021). Interlayer exciton mediated second harmonic generation in bilayer MoS_2. *Nat. Commun.* 12, 6894. doi:10.1038/s41467-021-27213-8

Sie, E. J., Lui, C. H., Lee, Y.-H., Fu, L., Kong, J., and Gedik, N. (2017). Large, valley-exclusive Bloch-Siegert shift in monolayer WS2. *Science* 355, 1066–1069. doi:10.1126/science.aal2241

Sousa, F. B., Lafeta, L., Cadore, A. R., Sahoo, P. K., and Malard, L. M. (2021). Revealing atomically sharp interfaces of two-dimensional lateral heterostructures by second harmonic generation. *2D Mater.* 8, 035051. doi:10.1088/2053-1583/ac0731

Sousa, F. B., Matos, M. J. S., Carvalho, B. R., Liu, M., Ames, A., Zhou, D., et al. (2024a). Giant Valley zeeman splitting in vanadium-doped WSe_2 monolayers. *Small* 20, 2405434. doi:10.1002/smll.202405434

Sousa, F. B., Nadas, R., Martins, R., Barboza, A. P. M., Soares, J. S., Neves, B. R. A., et al. (2024b). Disentangling doping and strain effects at defects of grown MoS_2 monolayers with nano-optical spectroscopy. *Nanoscale* 16, 12923–12933. doi:10.1039/D4NR00837E

Sousa, F. B., Zheng, B., Liu, M., Resende, G. C., Zhou, D., Pimenta, M. A., et al. (2024c). Effects of vanadium doping on the optical response and electronic structure of WS_2 monolayers. *Adv. Opt. Mater.* 12, 2400235. doi:10.1002/adom.202400235

Stepanov, E., Semin, S., Woods, C., Vandelli, M., Kimel, A., Novoselov, K., et al. (2020). Direct observation of incommensurate–commensurate transition in graphene-hbn heterostructures via optical second harmonic generation. *ACS Appl. Mater. and interfaces* 12, 27758–27764. doi:10.1021/acsami.0c05965

Sun, Z., Yi, Y., Song, T., Clark, G., Huang, B., Shan, Y., et al. (2019). Giant nonreciprocal second-harmonic generation from antiferromagnetic bilayer cri3. *Nature* 572, 497–501. doi:10.1038/s41586-019-1445-3

Trovatello, C., Marini, A., Xu, X., Lee, C., Liu, F., Curreli, N., et al. (2021). Optical parametric amplification by monolayer transition metal dichalcogenides. *Nat. Photonics* 15, 6–10. doi:10.1038/s41566-020-00728-0

Van Der Zande, A. M., Huang, P. Y., Chenet, D. A., Berkelbach, T. C., You, Y., Lee, G.-H., et al. (2013). Grains and grain boundaries in highly crystalline monolayer molybdenum disulphide. *Nat. Mater.* 12, 554–561. doi:10.1038/nmat3633

Virga, A., Ferrante, C., Batignani, G., De Fazio, D., Nunn, A. D. G., Ferrari, A. C., et al. (2019). Coherent anti-Stokes Raman spectroscopy of single and multi-layer graphene. *Nat. Commun.* 10, 3658. doi:10.1038/s41467-019-11165-1

Wang, G., Gerber, I. C., Bouet, L., Lagarde, D., Balocchi, A., Vidal, M., et al. (2015a). Exciton states in monolayer $MoSe_2$: impact on interband transitions. *2D Mater.* 2, 045005. doi:10.1088/2053-1583/2/4/045005

Wang, G., Marie, X., Gerber, I., Amand, T., Lagarde, D., Bouet, L., et al. (2015b). Giant enhancement of the optical second-harmonic emission of monolayers by laser excitation at exciton resonances. *Phys. Rev. Lett.* 114, 097403. doi:10.1103/physrevlett.114.097403

Wang, R., Chien, H.-C., Kumar, J., Kumar, N., Chiu, H.-Y., and Zhao, H. (2014). Third-harmonic generation in ultrathin films of mos2. *ACS Appl. Mater. and Interfaces* 6, 314–318. doi:10.1021/am4042542

Wen, X., Gong, Z., and Li, D. (2019). Nonlinear optics of two-dimensional transition metal dichalcogenides. *InfoMat* 1, 317–337. doi:10.1002/inf2.12024

Woodward, R. I., Murray, R. T., Phelan, C. F., de Oliveira, R. E. P., Runcorn, T. H., Kelleher, E. J. R., et al. (2016). Characterization of the second- and third-order nonlinear optical susceptibilities of monolayer MoS_2 using multiphoton microscopy. *2D Mater.* 4, 011006. doi:10.1088/2053-1583/4/1/011006

Wu, J.-B., Wu, H., and Tan, P.-H. (2024). Magneto-optical interactions in layered magnets. *Adv. Funct. Mater.* 34, 2312214. doi:10.1002/adfm.202312214

Xiao, D., Liu, G.-B., Feng, W., Xu, X., and Yao, W. (2012). Coupled spin and valley physics in monolayers of and other group-VI dichalcogenides. *Phys. Rev. Lett.* 108, 196802. doi:10.1103/PhysRevLett.108.196802

Xiao, D., Yao, W., and Niu, Q. (2007). Valley-contrasting physics in graphene: magnetic moment and topological transport. *Phys. Rev. Lett.* 99, 236809. doi:10.1103/physrevlett.99.236809

Xu, M., Ji, H., Zhang, M., Zheng, L., Li, W., Luo, L., et al. (2024). CVD synthesis of twisted bilayer WS_2 with tunable second harmonic generation. *Adv. Mater.* 36, 2313638. doi:10.1002/adma.202313638

Xu, X., Trovatello, C., Mooshammer, F., Shao, Y., Zhang, S., Yao, K., et al. (2022). Towards compact phase-matched and waveguided nonlinear optics in atomically layered semiconductors. *Nat. Photonics* 16, 698–706. doi:10.1038/s41566-022-01053-4

Yao, K., Zhang, S., Yanev, E., McCreary, K., Chuang, H.-J., Rosenberger, M. R., et al. (2022). Nanoscale optical imaging of 2D semiconductor stacking orders by exciton-enhanced second harmonic generation. *Adv. Opt. Mater.* 10, 2200085. doi:10.1002/adom.202200085

Yao, W., Xiao, D., and Niu, Q. (2008). Valley-dependent optoelectronics from inversion symmetry breaking. *Phys. Rev. B—Condensed Matter Mater. Phys.* 77, 235406. doi:10.1103/physrevb.77.235406

Yin, X., Ye, Z., Chenet, D. A., Ye, Y., O'Brien, K., Hone, J. C., et al. (2014). Edge nonlinear optics on a MoS_2 atomic monolayer. *Science* 344, 488–490. doi:10.1126/science.1250564

Yu, Q., Jauregui, L. A., Wu, W., Colby, R., Tian, J., Su, Z., et al. (2011). Control and characterization of individual grains and grain boundaries in graphene grown by chemical vapour deposition. *Nat. Mater.* 10, 443–449. doi:10.1038/nmat3010

Yuan, Y., Liu, P., Wu, H., Chen, H., Zheng, W., Peng, G., et al. (2023). Probing the twist-controlled interlayer coupling in artificially stacked transition metal dichalcogenide bilayers by second-harmonic generation. *ACS Nano* 17, 17897–17907. doi:10.1021/acsnano.3c03795

Zhang, Y., Yao, Y., Sendeku, M. G., Yin, L., Zhan, X., Wang, F., et al. (2019). Recent progress in cvd growth of 2d transition metal dichalcogenides and related heterostructures. *Adv. Mater.* 31, 1901694. doi:10.1002/adma.201901694

Zhao, M., Ye, Z., Suzuki, R., Ye, Y., Zhu, H., Xiao, J., et al. (2016). Atomically phase-matched second-harmonic generation in a 2D crystal. *Light Sci. and Appl.* 5, e16131. doi:10.1038/lsa.2016.131

Zipfel, W. R., Williams, R. M., and Webb, W. W. (2003). Nonlinear magic: multiphoton microscopy in the biosciences. *Nat. Biotechnol.* 21, 1369–1377. doi:10.1038/nbt899